Chemical Engineering Journal 474 (2023) 145318

Contents lists available at ScienceDirect

Chemical Engineering Journal

journal homepage: www.elsevier.com/locate/cej

The immunomodulatory effects of DNA-conjugated collagen scaffolds on bone healing

Jing-han Song [a,1], Jun-ting Gu [a,b,1], Gao-peng Dang [a,1], Zhi-ting Li [c], Chen Lei [a], Ling Li [a], Zhao Mu [a], Franklin R. Tay [d], Kai Jiao [a,e], Li-na Niu [a,*]

[a] State Key Laboratory of Oral & Maxillofacial Reconstruction and Regeneration & National Clinical Research Centre for Oral Diseases & Shaanxi Key Laboratory of Stomatology, Department of Prosthodontics, School of Stomatology, The Fourth Military Medical University, Xi'an, China
[b] National Translational Science Center for Molecular Medicine, Department of Cell Biology, State Key Laboratory of Cancer Biology, The Fourth Military Medical University, Xi'an, China
[c] Hubei University of Medicine, Shiyan, China
[d] The Dental College of Georgia, Augusta University, Augusta, GA, USA
[e] Department of Stomatology, Tangdu Hospital, Xi'an, China

ARTICLE INFO

Keywords:
Bone tissue regeneration
Collagen scaffold
DNA
Osteo-immunomodulation
Tregs

ABSTRACT

Unmodified collagen scaffolds represent a bottleneck in bone tissue engineering. Because of their limited mechanical and osteoinductive properties, these scaffolds do not perform well in repairing large bone defects. To overcome these limitations, a deoxyribonucleic acid-crosslinked collagen scaffold (DNA-Col) is fabricated to enhance healing of bone defects. The DNA-Col induces rapid formation of new bone tissue in a rat alveolar bone defect model. However, the improved osteogenic performance is not directly attributed to DNA-Col, but to the interaction between DNA-Col and T cells. Mechanistic experiments further demonstrate that recruitment of regulatory T cells (Tregs) is significantly triggered by implantation of DNA-Col *in vivo*. This is supported by the reversal of DNA-Col-induced bone regeneration after depletion of Tregs. These results indicate that Tregs play an important role in DNA-Col-induced new bone formation. Further investigations reveal that DNA-Col promotes Treg differentiation via metabolic reprogramming. These exciting findings establish the role of DNA-Col as a bioactive bone regeneration scaffold via its capability to interact with Tregs. The present study paths the way for creating smart hard tissue engineering materials with modulatory functions on the osteo-immunologic environment of a surgical bone defect.

1. Introduction

Large bone defects created by trauma, tumor resection, or infection do not heal easily in clinical practice[1]. To address this frustrating problem, clinical scientists have resorted to experimenting with new bone tissue engineering technology for improving the repair of these bone defects[2,3]. Graft materials utilized in bone tissue engineering include autografts, allografts, xenografts, and synthetic biomaterials[4]. Autografts are the "gold standard" for repairing bone defects and fractures. However, they suffer from drawbacks such as limited donor sources and donor site injury[2]. The use of allografts and xenografts is handicapped by their low osteoinductive capacity and high immunogenicity[5]. Hence, research on bioactive synthetic scaffolds have received much attention in the field of bone tissue engineering[6–8].

Incomplete healing of alveolar bone defects after tooth extraction is commonly seen in clinical dental practice[9]. This process causes an average of 40 to 60% bone loss during the first two years after tooth extraction[10]. Such an extent of bone loss adversely affects subsequent rehabilitative efforts, facial aesthetics, oral function, maxillofacial development, and even long-term health and quality of life. Therefore, regeneration of alveolar bone defects has always been a challenging endeavor[11]. Guided bone regeneration is usually used for reconstructing bone defects in which the cortical plates are lost[12,13]. Clinically, collagen scaffolds are the most commonly used biomaterials for guided bone regeneration[14]. Because pure collagen has poor osteoinductive properties, regeneration of defects that are filled with

* Corresponding author.
E-mail address: niulina831013@126.com (L.-n. Niu).
[1] These Authors contributes equally.

https://doi.org/10.1016/j.cej.2023.145318
Received 9 June 2023; Received in revised form 21 July 2023; Accepted 7 August 2023
Available online 26 August 2023

unmodified collagen scaffolds is far from satisfactory[15]. Hence, collagen scaffolds need to be modified to improve their functional properties.

Deoxyribonucleic acid (DNA) is a well-studied genetic material [16–17]. This biological polymer has also emerged as a nongenetic material for biomedical applications such as bone tissue regeneration [18,19]. The use of DNA in bone regeneration is based on its ability to: (i) bind calcium ions[20], (ii) promote biological apatite growth along its backbone[21,22], and (iii) act as an artificial extracellular matrix around osteoblasts to promote new bone formation *in vivo*[23,24]. The biocompatibility, biodegradability, high programmability, and osteoinductive potential of DNA renders it the holy grail of hard tissue engineering materials. Another non-genetic application of DNA is immunomodulation[25]. Deoxyribonucleic acids can be recognized by receptors on the surface of or within immune cells. Upon recognition, the DNAs ultimately trigger recruitment of immune cells that elicit immune responses[25]. Accordingly, DNA-modified biomaterials may possess immunomodulatory properties, and used for regulating tumor behavior[26]. However, less is known about the immunomodulatory effects of DNA-modified biomaterials on bone tissue engineering.

In light of the potential of DNA in improving the functional properties of collagen scaffolds, the present study investigated the use of DNA-modified collagen (DNA-Col) for bone repair, and examined the mechanism that is responsible for the improved osteogenesis exhibited this novel bioactive collagen-based scaffold. The null hypothesis tested was that there is no difference between an unmodified collagen scaffold and a DNA-Col scaffold in modulating the osteo-immunologic environment of a surgical bone defect to enhance bone regeneration.

2. Results

2.1. Characterization of DNA-Col

The phosphate backbone of DNA provides sites for conjugating other compounds to the biomacromolecule[18]. The 2D and 3D DNA-collagen scaffolds were constructed using 1-(3-dimethylaminopropyl)-3-ethylcarbodiimide hydrochloride (EDC)/N-hydroxy succinimide (NHS) crosslinking (Fig. 1a). The phosphate backbone of DNA is stainable with methyl green[20,27]. Accordingly, this cationic stain was used to stain DNA-Col and Col. The stained images showed that DNA-Col scaffolds were stained green, whereas pristine collagen scaffolds were unstained (Fig. 1b). Methyl green adsorption experiment showed that the content of DNA in the DNA-Col was 0.031 ± 0.006 μmol/g collagen. The 2D DNA-Col that was examined with immunofluorescence (Fig. 1c) showed co-labeling of collagen (COL-1 antibody, red) and DNA (nucleic acid dye, green); the observation was indicative of binding of DNA to the collagen matrix. X-ray photoelectron spectroscopy (XPS) revealed a tall peak that assigned to the phosphorus 2p orbital of DNA-Col (Fig. 1d). Analysis of DNA-Col scaffolds with energy-dispersive X-ray analysis (EDAX) identified increases in elemental phosphorous (Fig. 1e). Taken together, the aforementioned experimental results suggested binding of DNA to collagen. Scanning electron microscopy (SEM) of the DNA-Col showed linear structures resembling DNA that anchored to the collagen fibrils (Fig. 1f). The banded collagen structure was not damaged after chemical modification. The high magnification images of transmission electron microscope (TEM) and SEM showed that DNA was conjugated on the collagen (Fig. S2).

The modified collagen scaffolds were examined with attenuated total reflection-Fourier transform infrared spectroscopy (ATR-FTIR) to validate the crosslinking of DNA to collagen (Fig. 1f). Stretching vibrations in the infrared spectrum that were assigned to PO_3^{2-} (1063–1088 cm^{-1}) were indicative of the presence of DNA[28]. The peak at 973 cm^{-1}, assigned to the stretching vibration of the P–N–C bond, was indicative of the formation of stable chemical bonds between DNA and collagen [28,29]. Based on these information, the link between DNA and collagen is probably attributed to the interaction between the phosphate groups in DNA and the amino groups of collagen fibrils that produces irreversible phosphoramide bonds. After crosslinking, the tensile strength of DNA-Col was significantly higher than that of pure collagen (Fig. 1g).

2.2. Effect of DNA-Col on bone regeneration in vivo

A rat alveolar bone defect model was used to examine of DNA-Col on bone regeneration. The model was developed by extracting the maxillary right first molar from four-week-old Sprague-Dawley rats. Pristine collagen scaffolds or DNA-Col scaffolds were randomly implanted into each tooth socket. New bone formation was examined using micro-computed tomography (micro-CT) at the first week and the third week after surgery.

Representative sagittal and coronal slices taken from micro-CT images are shown in Fig. 2a. Red color in those images signified a higher level of bone mineral density. Red areas were visually larger in bone defects treated with DNA-Col. Quantitatively, both bone volume/total volume and bone mineral density in the DNA-Col-treated group were significantly higher, even at the first week (Fig. 2b and c). Coronal slices of micro-CT images were further used to evaluate the buccal and palatal height of the alveolar ridge. At the third week, the reduction of buccal and palatal height of the alveolar ridge was significantly less in DNA-Col-treated group (Fig. 2d). The results of Alizarin red S staining, hematoxylin-eosin staining, and immunofluorescent staining of the bone defect sites also showed that DNA-Col promoted osteogenesis *in vivo* (Fig. 2e, Fig. S3). Based on these *in vivo* evidence, DNA-Col has good potential in inducing bone regeneration.

2.3. Effect of DNA-Col on osteoblast differentiation in vitro

Bone mesenchymal stem cells were co-cultured with two-dimensional DNA-Col or pristine collagen (control). After osteogenic induction, alkaline phosphatase staining (ALP), Alizarin red S staining, and the expression of osteogenesis-related genes were examined. The results suggested there was no difference in each respective parameter between the experimental DNA-Col group and the control group (Fig. S4). Hence, it is reasonable to consider that there may be other factors involved in the DNA-Col-induced new bone formation.

2.4. Micro-environmental changes in DNA-Col-treated bone defects

Bulk-tissue RNA-sequence analysis was used to identify the “factors for promoting bone regeneration” that interacted with DNA-Col. From the rat alveolar bone defect model, implanted materials and the surrounding clot were harvested after 24 h of implant placement (n = 3 for each group). “Fragments per kilobase of transcript per million abundance values” were used to examine the specimens’ stability through correlation analysis (Fig. S5a). Correlation of gene expression levels between specimens is an important index to test the reliability of the experiments. Most of the correlation coefficients were within acceptable ranges (Fig. S5b). Principal component analysis of the data indicated that the DNA-Col specimens had notably different gene expression profiles, compared with the control Col specimens (Fig. S5c). There were extensive alterations in the gene expression profiles between DNA-Col and Col (Fig. 3a). Gene ontology analysis showed that DNA-Col induced up-regulation of genes that were associated with immune responses, especially the adaptive immune response (Fig. 3b). Differentially expressed genes (DEGs) were positively-correlated with those that are involved in T cell development, differentiation, and function. The DEGs related to T-cell activity appeared to be more regulatory in nature (Fig. 3c)[30–36]. In addition, genes responsible for pro-inflammatory activities were significantly down-regulated in the DNA-Col specimens [37–44] (Fig. 3c).

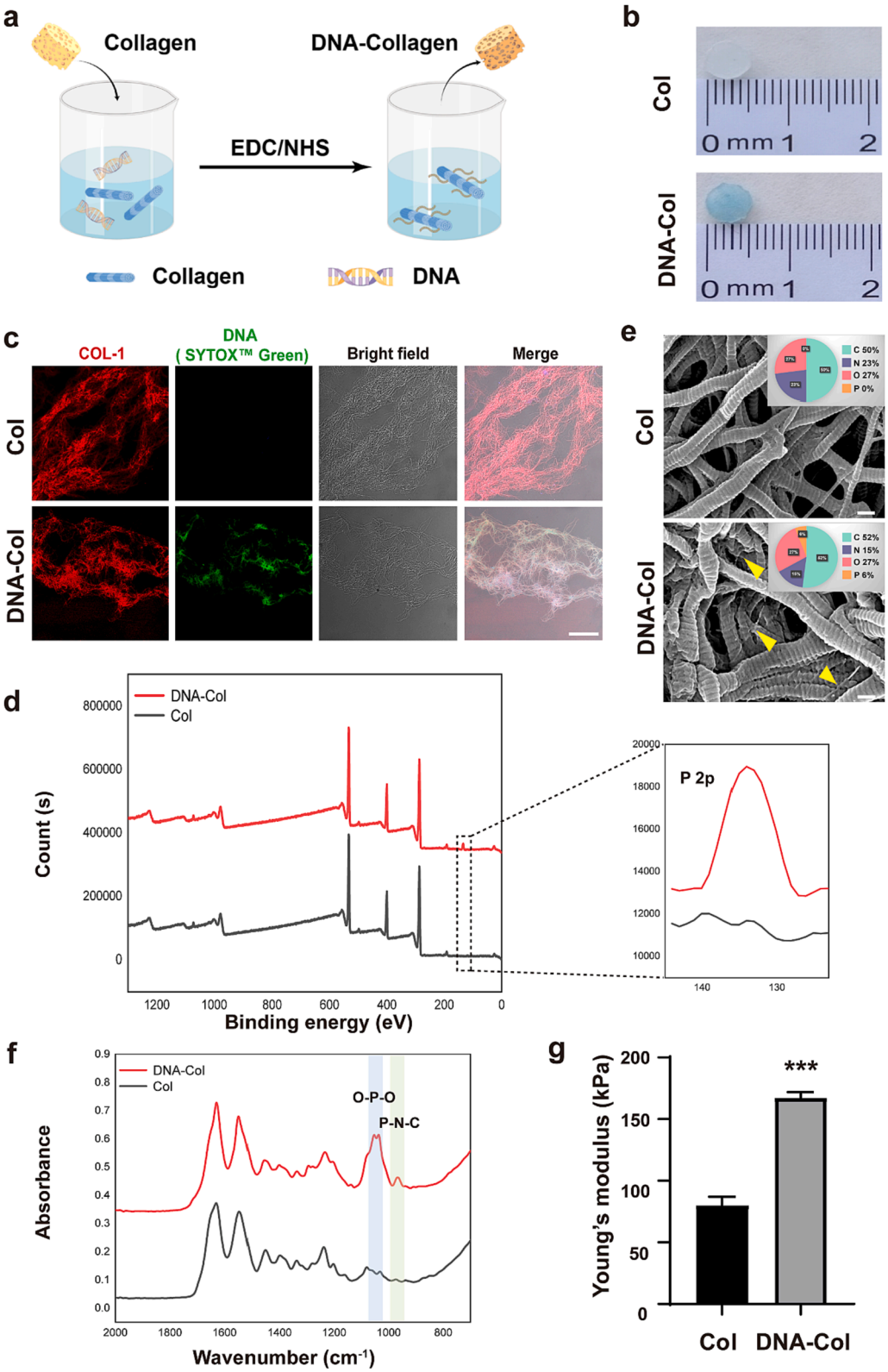

Fig. 1. Characterization of DNA-Col. **a**. Synthesis of DNA-Col. **b**. Methyl green staining of Col and DNA-Col. **c**. Characterization of 2D DNA-crosslinked collagen fibrils (2D DNA-Col). Confocal laser-scanning microscope images of 2D DNA-Col showing DNA (green) bound to pristine collagen fibrils (red). Bar = 50 μm. **d**. XPS survey spectrum of Col and DNA-Col. Inset shows enlargement of the P 2p region. **e**. SEM and EDAX elemental analysis of Col and DNA-Col (bar = 200 nm), yellow arrows: linear structures of DNA. **f**. ATR-FTIR spectra of Col and DNA-Col. **g**. Young's modulus of the different scaffolds (n = 3). DNA-Col, deoxyribonucleic acid modified-collagen scaffolds; Col, pristine collagen scaffolds; XPS, X-ray photoelectron spectroscopy; SEM, scanning electron microscopy; EDAX, energy-dispersive X-ray analysis; ATR-FTIR, attenuated total reflection-Fourier transform infrared spectroscopy. ***: $P < 0.001$ (Student's *t*-test).

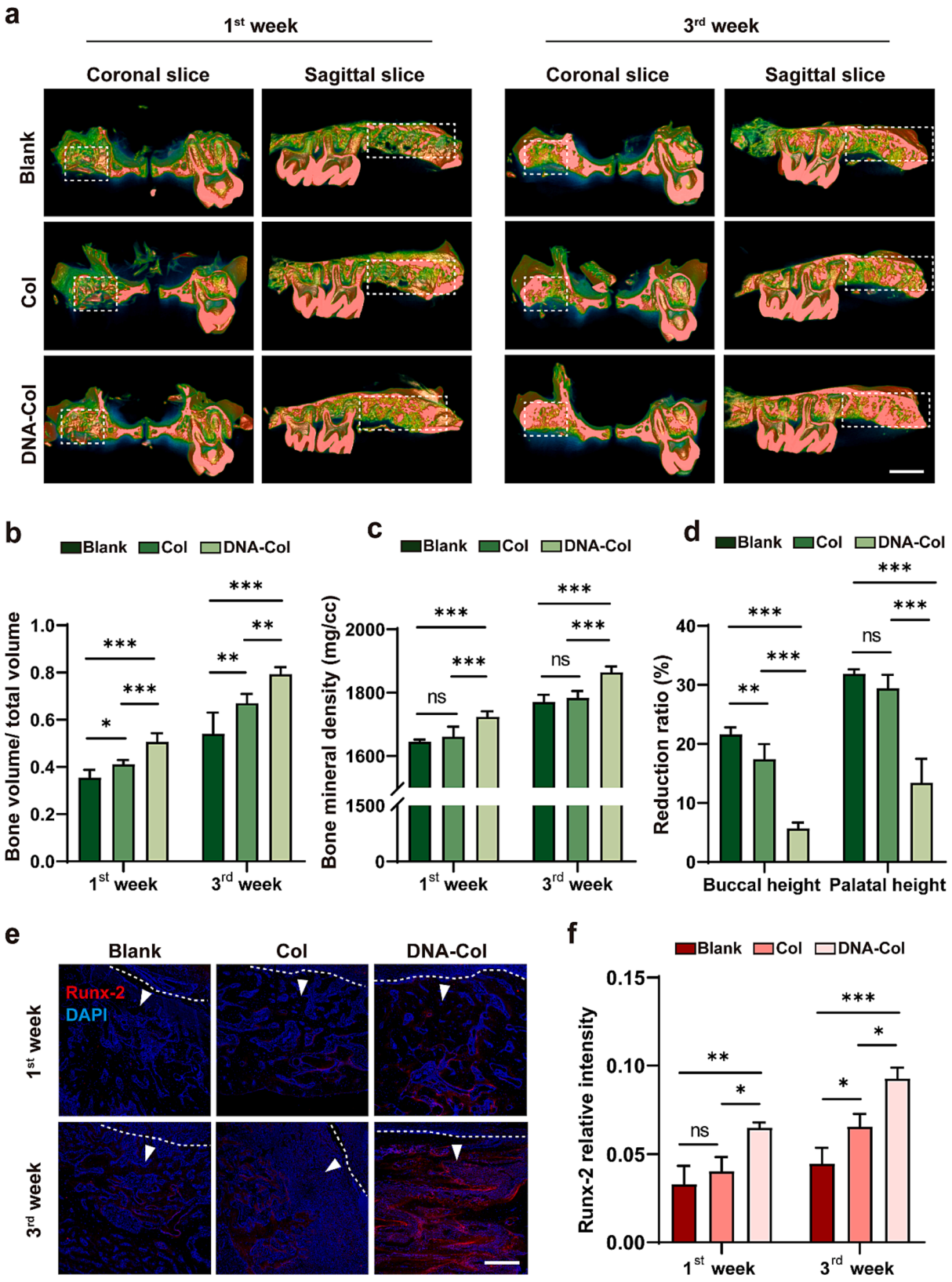

Fig. 2. Bone regeneration in the rat alveolar bone defect model. **a**. Micro-CT derived coronal and sagittal slices of the rat maxilla on the first and third week after surgery (bar = 2 mm). The white dashed box labeled the bone defect sites. **b**. Ratio of bone volume/total volume. **c**. Bone mineral density. **d**. Ratio of reduced buccal or palatal ridge height/ridge height. For (**b**), (**c**) and (**d**), parameters of the bone defect were calculated based on 3D reconstruction of micro-CT scans. **e**. Staining of Runx-2 of BMSCs at bone defect sites (bar = 250 μm). The dotted line represented the boundary between the bone tissue and the gingival tissue. The white arrows indicated the bone tissue. **f**. Quantitative analysis of the fluorescence intensity of Runx-2 in different groups (n = 3). Col, pure collagen; DNA-Col, deoxyribonucleic acid-modified collagen; micro-CT, micro computed tomography; Runx-2, Runt-related transcription factor 2. ***: $P < 0.001$, **: $P < 0.01$, *: $P < 0.05$, ns: no significance (one-way analysis of variance).

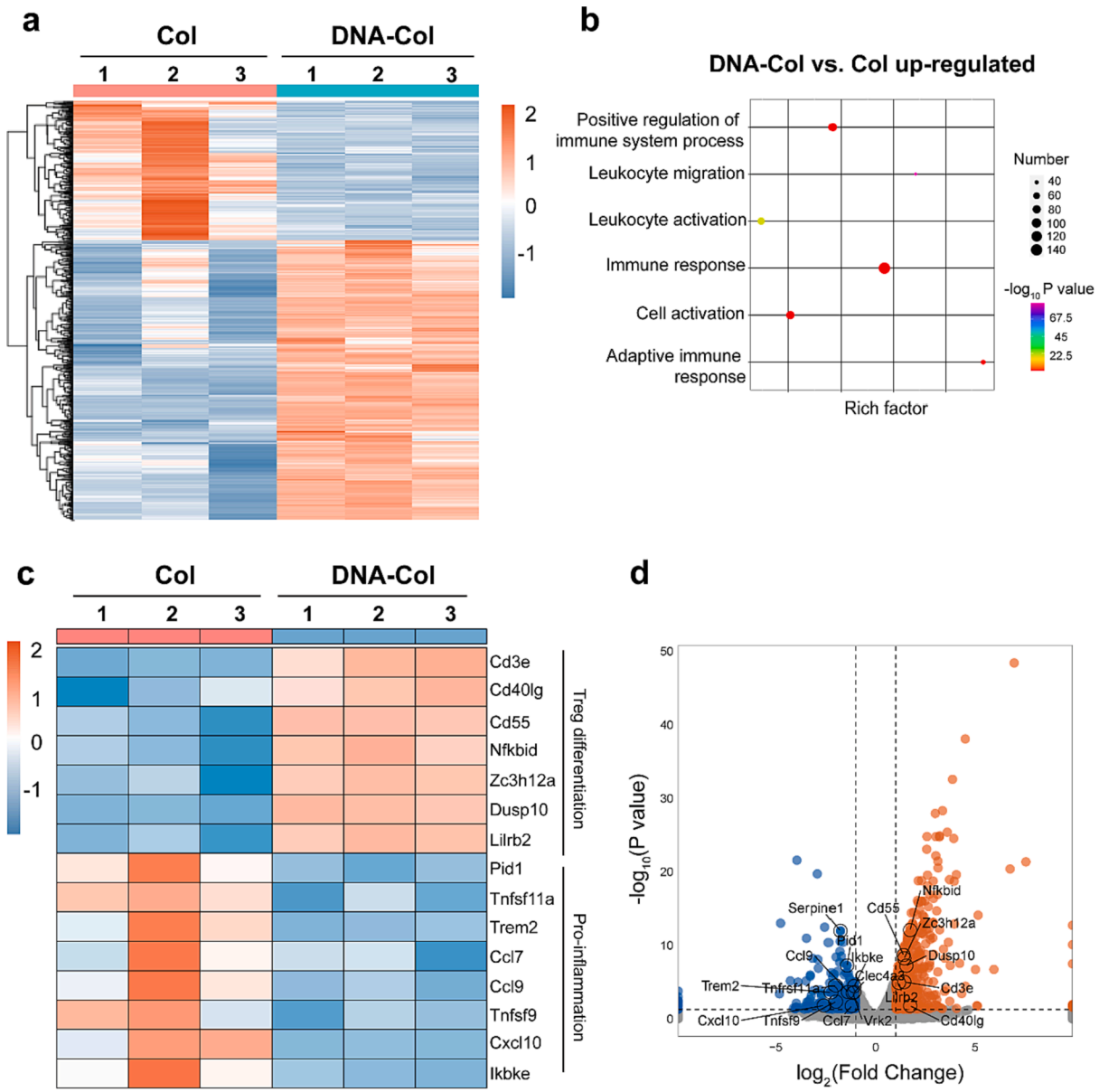

Fig. 3. The RNA sequence analysis of the material-clot complex. **a**. Heatmap of the differential genes of Col *vs* DNA-Col. **b**. Gene ontology analysis showing the positive regulation of adaptive immune system for DNA-Col. **c**. Heat map of T cell activity-related genes and inflammation-related genes in differentially expressed genes. **d**. Volcano plot of differentially expressed genes with all genes mentioned in (**c**) circled out. The dots in left or right represented significantly downregulated (blue dots) and upregulated (orange dots) differential genes. GO, gene ontology; Col, pure collagen; DNA-Col, deoxyribonucleic acid-modified collagen; CD3e, Cd3-epsilon; Cd40lg, Cd40 ligand; Nfkbid, nuclear factor kappa-B inhibitor delta; Zc3h12a, zinc finger CCCH-type containing 12A; Dusp10, dual specificity phosphatase 10; Lilrb2, leukocyte immunoglobulin like receptor B2; Pid1, phosphotyrosine interaction domain containing 1; Tnfsf9, tumor necrosis factor superfamily member; Trem2, triggering receptor expressed on myeloid cells 2; Ccl7, C-C motif chemokine ligand 7; Ccl9, C-C motif chemokine ligand 9; Tnfrsf11a, tumor necrosis factor receptor superfamily member 11a; Cxcl10, C-X-C motif chemokine ligand 10; Ikbke, inhibitor of nuclear factor kappa B kinase subunit epsilon.

2.5. Effect of DNA-Col scaffolds on recruitment of regulatory T cells (Tregs)

Based on the RNA sequence results, the authors conjectured that the number of Tregs was increased in DNA-Col scaffolds. Accordingly, CD4 (green), forkhead box protein P3 (Foxp3, red), and DAPI (blue) were used to label Tregs for examination with immunofluorescent microscopy. Representative images showed that the Col scaffolds displayed low-levels expression of CD4 and Foxp3, whereas DNA-Col scaffolds demonstrated robust accumulation of CD4, Foxp3, and regulatory T cells (Fig. 4a and b).

The proportion of Tregs was further examined with flow cytometry (Fig. 4c and d). The results indicated that the proportion of Tregs was significantly increased in the DNA-Col scaffolds ($P < 0.001$). Taken together, the immunofluorescence and flow cytometry results suggest that DNA-Col scaffolds enhance Treg recruitment.

2.6. Effect of Tregs on DNA-Col-induced bone regeneration

To determine whether Tregs were required for DNA-Col to promote bone regeneration, bone defects produced by tooth extraction were created in wild-type C57BL/6J mice and Treg-depleted C57BL/6J mice. Anti-CD25 antibodies were injected to deplete Tregs in the C57BL/6J mice (Fig. 5a). After injection, the number of Tregs was significantly reduced ($P < 0.001$). The depleting effect was maintained until the 21st day (Fig. 5b). After Treg depletion, bone regeneration in both DNA-Col

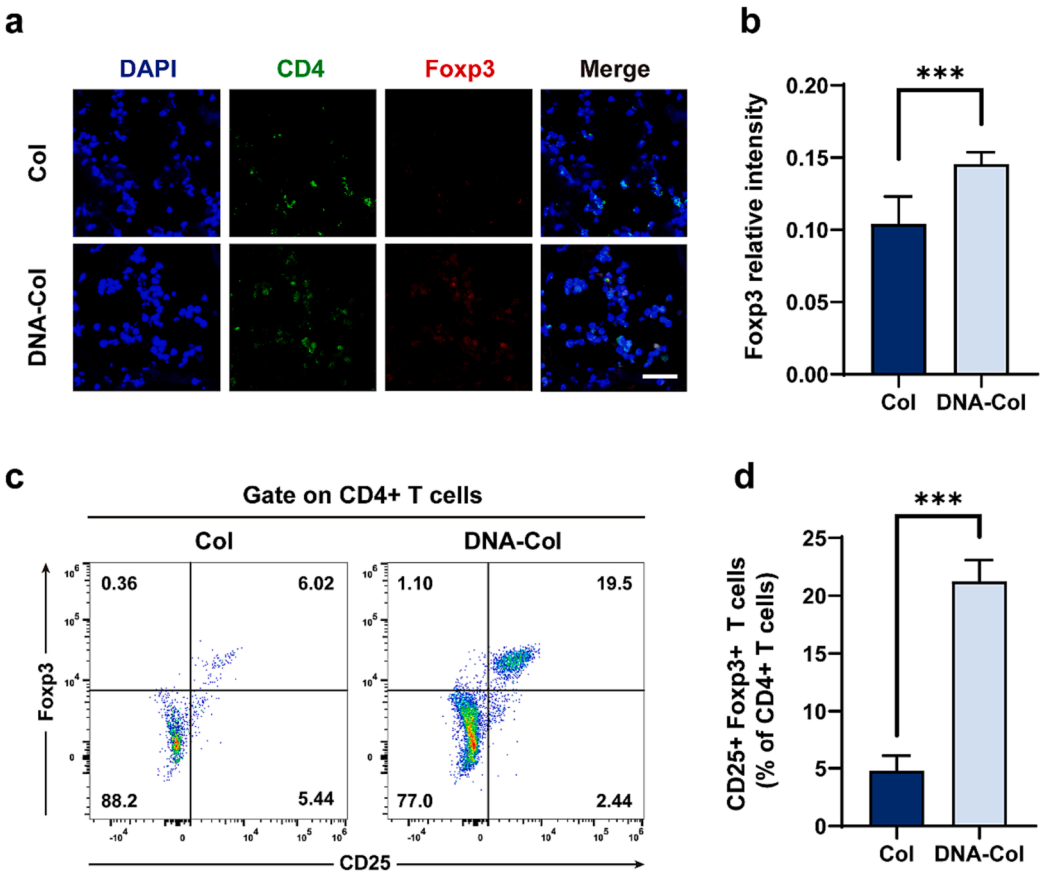

Fig. 4. Enrichment of Tregs induced by DNA-Col *in vivo*. **a**. Representative examples of confocal immunofluorescence imaging for DAPI, CD4, Foxp3 in Col or DNA-Col from tooth sockets of rats (bar = 35 μm). **b**. Quantitative analysis of the fluorescence intensity of Foxp3 expression in different groups (n = 6). **c-d**. Flow cytometry of Treg markers in the Col or DNA-Col scaffolds implanted into from rat tooth sockets (n = 4). Col, pristine collagen; DNA-Col, deoxyribonucleic acid-modified collagen; Tregs, regulatory T cells; Foxp3, forkhead box protein P3. ***: $P < 0.001$ (Student's *t*-test).

and Col groups was reduced. Moreover, the excellent osteogenic performance of DNA-Col was diminished after inhibition of Tregs (Fig. 5d and e). Taken together, the results confirms that DNA-Col induces new bone formation through the activity of Tregs.

2.7. Mechanism whereby DNA-Col promoted Treg differentiation

The role that Tregs played in DNA-Col-induced bone regeneration was also confirmed in a Treg-depleted murine model. These observations prompted the authors to examine if there is interaction between DNA-Col and increased Tregs. The hypothesis put forward was that DNA-Col affects Tregs at the level of their differentiation.

Regulatory T cells may be differentiated *in vitro* from naïve CD4+T cells in the presence of transforming growth factor-β (TGF-β) and interleukin-2 (IL-2). Hence, CD4+T cells were isolated and co-cultured with DNA-Col or Col in the presence of TGF-β and IL-2 (Fig. 6a). Flow cytometry performed after 24 h identified that Treg differentiation was significantly amplified in the DNA-Col group (Fig. 6d and e). Immunofluorescence analysis showed a corresponding increase in the level of Foxp3 in the DNA-Col group (Fig. 6b and c). The DNA-Col group also exhibited enhanced secretion of IL-4 and IL-10 (Fig. 6f and g). Taken together, these evidence demonstrate that DNA-Col possesses an immunomodulatory effect. The DNA-Col scaffold promotes Treg differentiation and contributes to establishing an anti-inflammatory microenvironment.

Previous studies have shown that DNA released from neutrophil extracellular traps facilitate Treg differentiation by promoting mitochondrial oxidative phosphorylation (OXPHOS) of CD4+T cells[45]. The results of these studies indicate that DNA-Col may reprogram the metabolic process of CD4+T cells by promoting OXPHOS to render the T cells more regulatory in function. Accordingly, TEM was used to observe the mitochondria of CD4+T cells. Co-culture of CD4+T cells with DNA-Col increased the number of mitochondria with tight cristae in the CD4+T cells (Fig. 7a). In a subsequent experiment, peroxisome proliferator-activated receptor-γ coactivator-1α (PGC-1α), the master regulator of mitochondrial biogenesis, was analyzed with western blot. The CD4+T cells that were treated with DNA-Col showed significantly up-regulation of PGC-1α expression (Fig. 7b). Because upregulation of PGC-1α promotes OXPHOS of CD4+T cells, the TEM and western blot results suggested that DNA-Col might affect the mitochondria-related metabolic process of CD4+T cells.

The balance between OXPHOS and glycolysis has been shown to be critical for Treg differentiation[46]. To clarify this issue, CD4+T cells were co-cultured with DNA-Col or Col for quantifying the mitochondrial oxygen consumption rate (OCR) and extracellular acidification rate (ECAR) to reflect the mitochondrial respiration and glycolytic rate, respectively. The DNA-Col treated CD4+T cells had significantly increase in basal respiration, maximal respiration, and spare respiratory capacity (Fig. 7c). There was no noticeable difference in ECAR between the DNA-Col and Col groups (Fig. 7d). Taken together, these data indicate that DNA-Col promotes Treg differentiation by facilitating OXPHOS of CD4+T cells. However, the mechanism whereby DNA-Col affects OXPHOS remains unknown.

2.8. Mechanism whereby DNA-Col induces metabolic reprogramming of CD4+T cells

Previous studies reported that activation of Toll-like receptor 4 (TLR4) up-regulates PGC-1α through the phosphorylation of mitogen-activated protein kinases 38 (p38)[47]. Toll-like receptor 4 is a well-known pattern recognition receptor that is involved in adaptive immune response[48]. This receptor promotes the activation of CD4+T cells and helps to maintain the expansion and function of Tregs[45]. Hence, *in vitro* and *in vivo* experiments were designed to detect whether

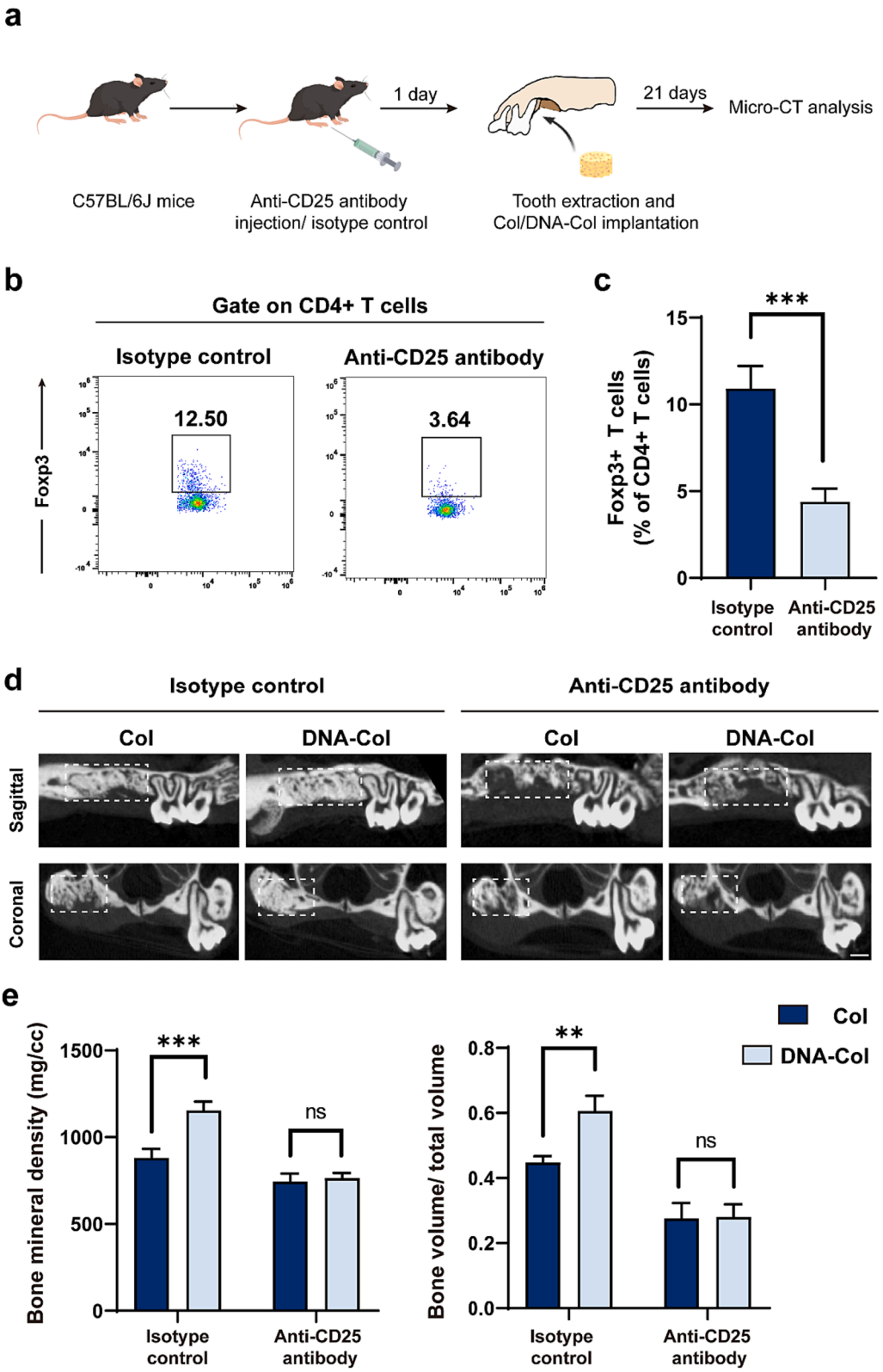

Fig. 5. Inhibition of Tregs prevented bone regeneration in the DNA-Col group. **a**. Experimental design for *in vivo* examination of the role of Tregs in DNA-Col-induced osteogenesis, using anti-CD25 antibodies. **b-c**. The efficiency of Treg depletion by anti-CD25 antibodies injection was evaluated with flow cytometry (n = 3). **d**. Sagittal and coronal slices derived from micro-CT scans of each group, on the third week after tooth extraction (bar = 500 μm). **e**. Bone mineral density and ratio of bone volume/total volume in the tooth sockets. The parameters were calculated based on 3D reconstruction of micro-CT scans (n = 4). Col, pure collagen; DNA-Col, deoxyribonucleic acid-modified collagen; micro-CT, micro computed tomography. **: $P < 0.01$, ***: $P < 0.001$, ns: no significance (Student's *t*-test, one-way analysis of variance).

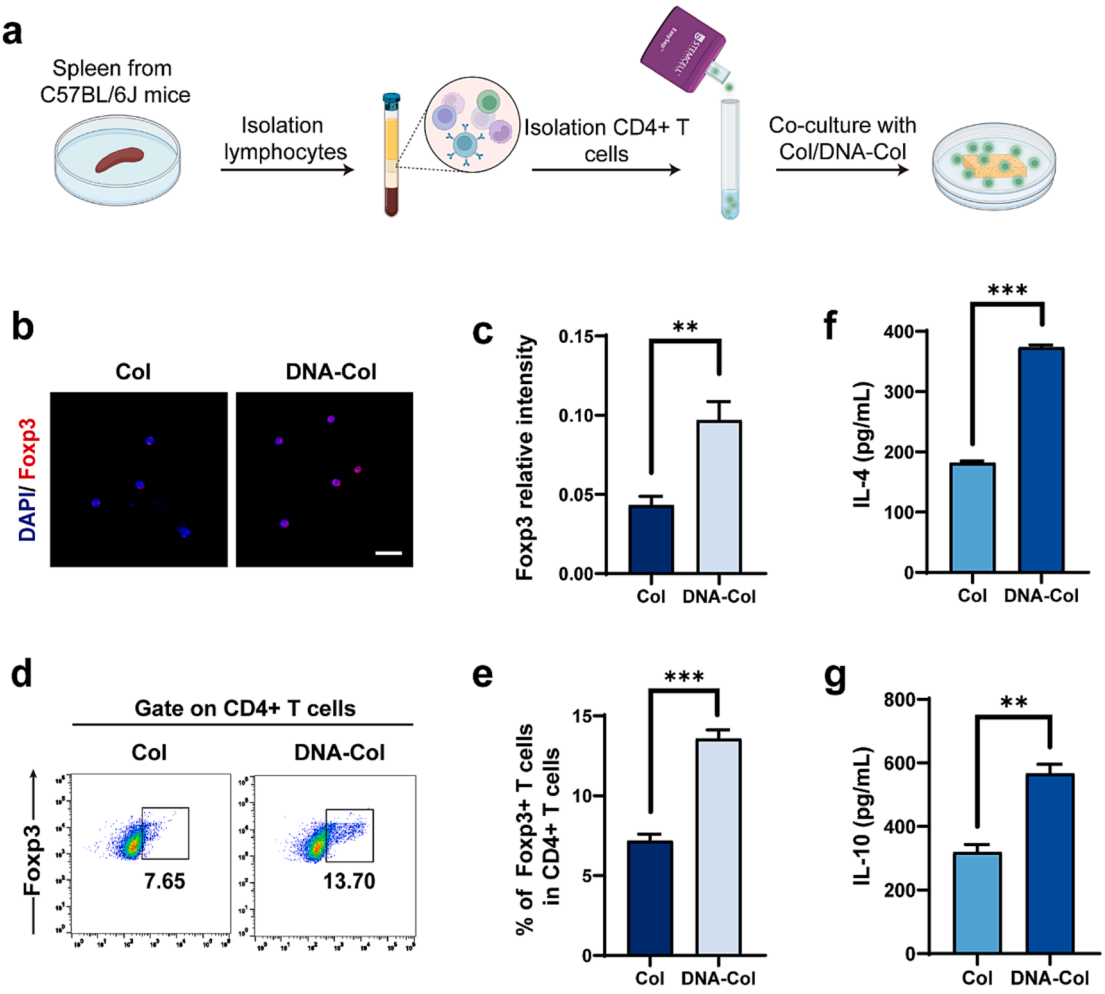

Fig. 6. DNA-Col promoted Treg differentiation, and secretion of IL-4 and IL-10 *in vitro*. **a**. Design of the *in vitro* experiments. **b**. Representative examples of immunofluorescence showing the expression of Foxp3 (red) and DAPI (blue) in different co-culture groups. Bar = 30 μm. **c**. The data in (b) were analyzed quantitatively (n = 6). **d-e**. Flow cytometry showing Treg differentiation induced by DNA-Col (n = 6). **f-g**. Enzyme-linked immunosorbent assay for production of IL-4 and IL-10 in cell-free supernatants (n = 6). Col, pure collagen; DNA-Col, deoxyribonucleic acid-modified collagen; IL-4, interleukin 4; IL-10, interleukin 10; Foxp3, forkhead box protein P3. **: $P < 0.01$, ***: $P < 0.001$ (Student's *t*-test).

DNA-Col up-regulated PGC-1α expression in CD4+T cells via the TLR4-p38-PGC-1α pathway (Fig. 8a).

The CD4+T cells that were treated *in vitro* with TAK-242 were designated as the TLR4 inhibition group. The CD4+T cells that were treated with the same volume of dimethyl sulfoxide were designated as the control group. Immunofluorescence and western blot results confirmed that DNA-Col promoted PGC-1α expression, but this promoting effect was diminished with debilitation of phosphorylated p38 after treatment with TAK-242 (Fig. 8b and c, e).

To determine whether the Treg differentiation-promoting effect of DNA-Col depended on the activation of TLR4, C57BL/6J mice injected with TAK-242 or DMSO were divided into the TLR4 inhibition group and control group, respectively. Both groups underwent extraction of the maxillary right first molar and were implanted with DNA-Col or Col. The proportion of Tregs in DNA-Col and Col scaffolds was examined 24 h after scaffold implantation (Fig. 8a). The result showed that Treg differentiation was significantly reduced in the TLR4 inhibition group (Fig. 8d and f). Taken together, the results indicates that DNA-Col promotes Treg differentiation via the activation of the TLR4-p38-PGC-1α pathway.

3. Discussion

Bone tissue engineering materials are favorable alternatives to autografts for promoting the repair of bone tissue defects. The present study developed a modified collagen scaffold by conjugating DNA to collagen. Experiments were conducted to demonstrate the superiority of DNA-Col over pristine collagen as a bioactive scaffold for bone regeneration. The improved bone defect healing relies on the immunomodulatory effect of DNA-Col on the surgical defect microenvironment.

Because of its poor mechanical property, a pristine collagen scaffold is incapable of maintaining the defect space for bone regeneration; as a result, its development has reached a bottleneck in the field of bone tissue engineering[15]. Crosslinking technology has the potential to improve the mechanical properties of fibrillar collagen[49]. Accordingly, chemical crosslinking was used in the present study to increase the modulus of elasticity of collagen scaffolds to meet the requirement of a bone repair biomaterial.

Although DNA-Col effectively promoted new bone formation in rat alveolar bone defects. The modified collagen material did not promote osteogenic differentiation when co-cultured with bone marrow stem cells. Phosphate degradation from DNA has been reported to be a promoter for osteogenic differentiation[23]. The inconsistent *in vivo* and *in vitro* results may be attributed to the covalent interaction between DNA and collagen, which slows down the release of phosphate from the DNA backbone (Fig. S6). As a result, DNA-Col did not show acceptable osteogenic performance *in vitro*. The inconsistency between *in vitro* and *in vivo* results suggests that the interaction of DNA-Col and the bone defect

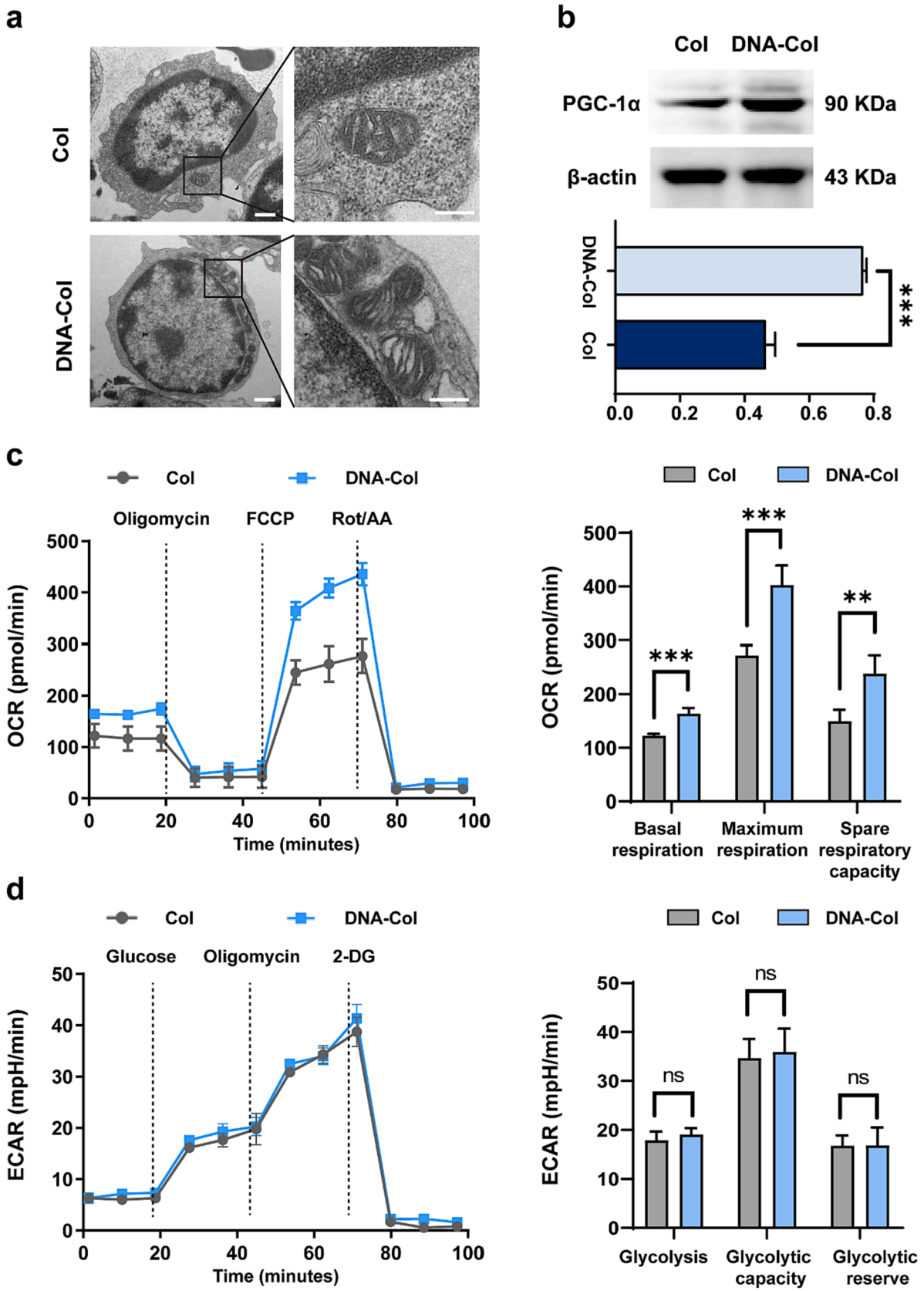

Fig. 7. DNA-modified collagen promoted mitochondrial oxidative phosphorylation in CD4+T cells. **a**. TEM of the number and shape of mitochondria present in CD4+T cells. Images on the right (bar = 500 nm) are high magnification views of the boxed areas in the left images (bar = 1 μm). **b**. Western blot and quantitative analysis of PGC-1α expression (n = 3). **c**. Oxygen consumption rate (OCR) of CD4+T cells (n = 3). **d**. Extracellular acidification rate (ECAR) rate of CD4+T cells (n = 4). Col, pure collagen; DNA-Col, deoxyribonucleic acid-modified collagen. PGC-1α, peroxisome proliferator-activated receptor-γ coactivator-1α; FCCP, carbonyl

cyanide-4-(trifluoromethoxy) phenylhydrazone; Rot/AA, rotenone and antimycin A; 2-DG, 2-deoxy-D-glucose. **: $P < 0.01$, ***: $P < 0.001$, ns: no significance (Student's *t*-test).

microenvironment may be the contributor.

Immune responses play a crucial role in bone healing[50]. An inflammatory cascade is first initiated by tissue damage[51]. During the healing phase, a switch from a pro-inflammatory to an anti-inflammatory environment is required to support bone regeneration [51]. Results of RNA sequencing suggest that DNA-Col induces up-regulation of genes associated with adaptive immune response. Interestingly, the DEGs specifically involved in Treg development, differentiation, and function were positively-correlated, while genes related to pro-inflammation were negatively-correlated. Regulatory T cells are identified as critical regulators in the initial phase of bone defect healing [52]. The number of Tregs was increased from 24 h onwards during the initial healing phase[52]. Correspondingly, anti-inflammatory cytokines released from Tregs (i.e., IL-4 and IL-10) were up-regulated to provide an anti-inflammatory environment for osteogenesis[52].

It has been reported that reduction of Tregs causes delayed fracture healing[53], while infusion of Tregs markedly improves bone regeneration[54]. Mechanistically, Tregs secret anti-inflammatory factors, such as IL-10 and IL-4, thereby promoting osteogenic differentiation[55]. Because the DNA-Col scaffold enhanced Treg recruitment in the present study, it is highly likely that the improved bone regeneration is attributed to Treg activities. This notion was further supported by reversal of the osteogenesis promotion potential of DNA-Col after Treg inhibition *in vivo*. In vitro, the conditioned medium of DNA-Col with T cells was able to significantly promote osteogenic differentiation (Fig. S7).

A recent study demonstrated that DNA released from neutrophil extracellular traps promotes the differentiation of T cells into Tregs with anti-inflammatory properties[45]. In the present study, the authors confirmed that DNA-Col promoted Treg differentiation and contributed to the secretion of IL-4 and IL-10 *in vitro*. Mechanistically, the DNA-Col scaffold increased the number of mitochondria in CD4+T cells and up-regulated the expression of PGC-1α. Interestingly, DNA-Col mediated enhanced OXPHOS. According to the literature, differentiation of T cells into Tregs requires metabolic reprogramming that favors oxidative phosphorylation[45]. The present data demonstrated that DNA-Col reprogrammed the metabolic processes of CD4+T cells, tilting the balance toward OXPHOS to promote Treg differentiation.

As a key contributor to mitochondrial biogenesis, PGC-1α is up-regulated to directly enhance OXPHOS[56]. A previous study demonstrated that activation of TLR4 on cell membranes promotes the expression of PGC-1α through the phosphorylation of p38[47]. Notably, TLR4 is linked to the differentiation of Tregs[57], which is promoted by OXPHOS[45]. The encouraging results derived from those studies prompted the authors to investigate the pathway involved in DNA-Col induced Treg differentiation. The use of a TLR4 inhibitor (TAK-242) *in vitro* undermined the ability of DNA-Col to stimulate PGC-1α expression and p38 phosphorylation. Moreover, inhibition of TLR4 induced notable reduction of Tregs in the DNA-Col scaffold. These observations further imply that DNA-Col causes metabolic reprogramming of CD4+T cells via the TLR4-p38-PGC-1α pathway.

However, there are some limitations in the present study. Firstly, the immunomodulatory and osteogenic effects of DNA-Col are only tested in alveolar bone defects. Because of the existence of potentially dissimilar immune microenvironments and osteogenic properties in different bone defects, the immunomodulatory and osteogenic performance of DNA-Col need to be verified in other bone defect models. Of note, DNA-Col exhibits enhanced mechanical properties when compared with collagen scaffolds. Whether the immunomodulatory property of DNA-modified collagen is related to the change in mechanical properties requires further investigations. Because of its low tensile modulus, DNA-Col is more suitable for repair of low load-bearing bone defects. The mechanical strength of DNA-Col needs further improvement for it to be used as a load-bearing scaffold in cortical bone replacement. Another critical limitation of the present work is that the connection between immune regulation and bone regeneration was not fully established; antigen-specific, adaptive immune response was not analyzed and should be done in future studies. In addition, it is not clear which DNA property (e.g., sequence, length, structure, or concentration) is more important in its interaction with TLR4. Last but not the least, the methods to maintain the properties of DNA in DNA-Col deserve further exploration.

4. Conclusion

Binding of DNA onto a collagen scaffold via crosslinking endows the modified collagen scaffold with excellent bone regeneration potential. The DNA-Col scaffold improves osteogenesis via the modulation of Tregs. This modulation is achieved through the TLR4-p38-PGC-1α pathway. Implantation of DNA-Col scaffolds represents an efficient therapeutic method that regulates Tregs and promotes bone defect healing. The present study emphasizes osteo-immunomodulation in bone tissue engineering, with the aim of addressing clinical bottlenecks in the near future.

5. Materials and methods

Supplementary Fig.1 summarizes the experimental design of the present study. Additional materials and methods were listed in the Supplementary Information.

5.1. Deoxyribonucleic acid-crosslinked collagen scaffolds (DNA-Col)

5.1.1. Preparation of DNA-Col

Calf thymus deoxyribonucleic acid (DNA, MilliporeSigma, Burlington, MA, USA) was cross-linked with collagen scaffolds (Ace Surgical Supply Co., Inc., MA, USA). Because the maximum solubility of DNA is 1 mg/mL, 5 mg of DNA was dissolved in 5 mL of 0.1 M 2-(N-morpholino)-ethanesulfonic acid buffer (MES, pH 6.0). 62.5 mg of 1-(3-dimethylaminopropyl)-3-ethylcarbodiimide hydrochloride (EDC) and 75 mg of N-hydroxy succinimide (NHS) were mixed in the DNA-MES solution. The pH of the mixture was increased to 7.3 using concentrated phosphate-buffered saline (PBS; pH 7.2–7.5). Commercially available collagen scaffolds purchased from Iregene (Beijing, China) were cut into cylinders, each with a diameter of 5 mm and thickness of 2 mm. After 30 min, the collagen scaffolds were incubated in the DNA/EDC/NHS cross-linking solution. This process lasted for 2 h at room temperature and was protected from light. The DNA-modified collagen scaffolds were subsequently washed in DNase-free water. They were then frozen at − 80 °C and freeze-dried to produce DNA-modified collagen (DNA-Col).

5.1.2. Preparation of DNA-conjugated self-assembled collagen fibrils (2D DNA-Col)

Collagen fibrils were self-assembled from rat tail tendon-derived collagen/acetic acid stock solution (5 mg/mL) using the dialysis method[7]. The self-assembled collagen solution was placed on a dish and air-dried. A DNA, EDC, and NHS mixed was prepared as previously described and added to the collagen-containing dish. After incubating for 2 h, the dish was rinsed with DNase-free water and air-dried.

5.1.3. Methyl green staining of DNA-Col

Methyl green is a basic dye that binds with DNA[29]. Deoxyribonucleic acid-modified collagen scaffolds and pristine collagen scaffolds (Col) with a diameter of 5 mm were immersed in a 2% methyl green (Macklin, Shanghai, China) for 5 min. Both the DNA-Col and Col

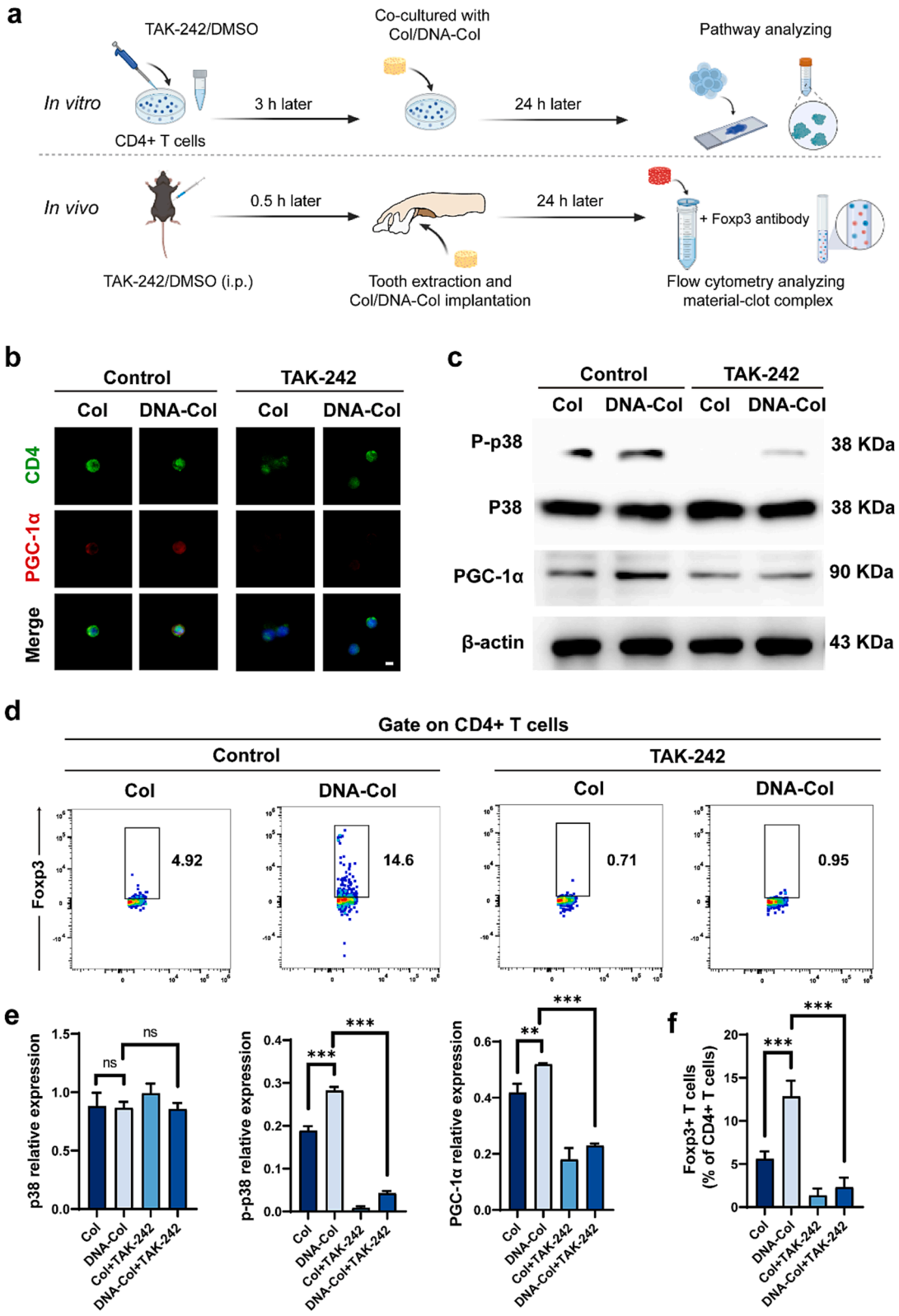

Fig. 8. DNA-conjugated collagen reprogramed the metabolic process of CD4+T cells via the TLR4-p38-PGC-1α pathway. **a**. Experimental design of the *in vitro* and *in vivo* models. **b**. Immunofluorescence staining of TAK-242 or DMSO pretreated T cells that were co-cultured with Col or DNA-Col. Cell nuclei were stained blue, PGC-1α was stained red, and CD4 was stained green. Bar = 5 μm. **c** and **e**. Western blot and corresponding quantitative analysis of the expression of p38, p-p38, and PGC-1α after treatment with Col or DNA-Col in the TLR4 inhibited group or the control group (n = 3). **d** and **f**. Flow cytometry of the Treg markers in Col or DNA-Col that were implanted into the tooth sockets of TLR4 inhibited mice or control mice (n = 4). DMSO, dimethyl sulfoxide; TAK-242, Toll-like receptor 4 inhibitor; Col, pure collagen; DNA-Col, deoxyribonucleic acid-modified collagen; Tregs, regulatory T cells; PGC-1α, peroxisome proliferator-activated receptor-γ coactivator-1α; p38, a form of mitogen-activated protein kinases; p-p38, phospho-p38. **: $P < 0.01$, ***: $P < 0.001$, ns: no significance (one-way analysis of variance).

scaffolds were thoroughly rinsed with Milli-Q water until the rinse solution was colorless.

5.1.4. Attenuated total reflection-Fourier transform infrared spectroscopy

Functional groups in the DNA-Col and Col were measured using an attenuated total reflection-Fourier transform infrared spectroscopy (ATR-FTIR; FTIR-8400S, Shimadzu, Tokyo, Japan). Infrared spectra were produced using 32 scans with a resolution of 4 cm^{-1} over the range of 4000–400 cm^{-1}.

5.1.5. X-ray photoelectron spectroscopy

X-ray photoelectron spectroscopy (XPS; K-Alpha, ThermoFisher Scientific, Waltham, MA, USA) was used to analyze the surface elements of Col and DNA-Col.

5.1.6. Scanning electron microscopy and energy-dispersive X-ray analysis

The surface morphology of Col and DNA-Col were characterized with a scanning electron microscope (SEM, S-4800, Hitachi, Tokyo, Japan) at 5 kV. The specimens were dehydrated with an ascending ethanol series (50%, 70%, 80%, 90%, and 100%) for 15 min each, and finally suspended in hexamethyldisilane for 30 min. The chemically-dehydrated specimens were air-dried and sputter-coated with gold/palladium prior to examination. Elemental analysis was performed by energy dispersive X-ray spectroscopy (EDAX).

5.1.7. Immunofluorescence

Slides coated with reconstituted type I collagen fibrils and 2D DNA-Col were labeled with collagen-I rabbit anti-rat antibody (Ab34710, Proteintech, Wuhan, Hubei, China), SYTOX™ Green (S34860, ThermoFisher Scientific, Waltham, MA, USA), and Alexa Fluor 594 goat anti-rabbit secondary antibodies (33112ES60, Yeasen Biotechnology, Shanghai, China). After rinsing with PBS, the slides were examined with confocal laser-scanning microscopy (Leica Microsystems, Wetzlar, Hesse, Germany).

5.1.8. Young's modulus

The modulus of elasticity of the Col and DNA-Col scaffolds was determined using a uniaxial compression test. Experiments were conducted in triplicate. The Young's modulus of the specimens was tested using a universal tensile tester (EZ-SX, Shimadzu, Japan). The dried specimens were cut into blocks of 50 mm × 5 mm × 2 mm. Each block was held by the grips of the universal tensile tester. The distance between grips was adjusted to 10 mm. The separation speed between grips was set at 1 mm/min. A tensile load was applied until the collagen specimen delaminated. Young's modulus was calculated using the formula: maximum load/(displacement × cross-sectional area).

5.2. Bone regeneration in vivo and in vitro

5.2.1. Rat alveolar bone defect model

Four-week-old Sprague-Dawley rats were obtained from the Laboratory Animal Research Center of the Fourth Military Medical University, Xi'an, China and kept under specific pathogen-free conditions. Animal experiment was conducted at the Experimental Animal Center of the Fourth Military Medical University. All protocols were performed in accordance with the Guidelines for Care and Use of Experimental Animals of the university. The research protocols were approved by the Medical Ethics Committee of the university (#20220905).

A rat alveolar bone defect model was used to evaluate the osteogenic property of the DNA-Col. 6- to 8-week-old male Sprague-Dawley rats (n = 36) were used in this experiment. The size of Col and DNA-Col used for animal experiments was 5 mm in diameter and 2 mm in thickness. General anesthesia was administered via intraperitoneal injection of pentobarbital sodium (50 mg/kg). The maxillary right first molar was extracted in a minimally invasive manner. A standardized defect was created immediately after tooth extraction, using a 1.4 mm-diameter dental bur to remove the inter-radicular septum of the maxillary right first molar. The DNA-Col or Col scaffold was grafted into the tooth socket. Tooth sockets without grafts were used as blank control. The adjacent mucosa was subsequently sutured[29].

5.2.2. Micro-computed tomography (Micro-CT)

The rats were sacrificed at the first and third week after surgery by intraperitoneal injection of excessive pentobarbital sodium (n = 6). The maxillary bones were collected and fixed in 4% paraformaldehyde for 48 h. The specimens were scanned using micro-CT (Inveon, Siemens Preclinical, Knoxville, TN, USA) at high resolution. Images were reconstructed into a three-dimensional structure and analyzed using the Inveon Research Workplace software. Briefly, sagittal slices were used to evaluate new bone formation in the tooth sockets. The reference views were set to best present the mesial and distal canals of maxillary right second molar. New bone volume fraction (bone volume/total volume) and bone mineral density in the tooth sockets were analyzed. The region of interest was set as 2 mm × 1 mm × 1 mm. In addition, coronal slices were used to evaluate the buccal and palatal height of the alveolar ridges. The range of alveolar ridge height was from the upper-most to the bottom-most of the alveolar ridge.

5.2.3. In vitro osteogenesis of DNA-Col

5.2.3.1. Cell culture. Murine bone mesenchymal stem cells (mBMSCs) were purchased from Cyagen Biosciences (Guangdong, China). The cell culture medium was α-MEM (Gibco, ThermoFisher Scientific, Waltham, MA, USA), supplemented with 10% fetal bovine serum and 1% penicillin/streptomycin (Invitrogen, ThermoFisher Scientific). The mBMSCs were seeded on 2D and 3D models of Col and DNA-Col. The specimens were subsequently incubated with 5% CO_2 at 37 °C. After the mBMSCs reached 80% confluence, the culture medium was change to an osteogenic medium containing 10 nM dexamethasone, 4 mM β-glycerophosphate, and 50 mg/mL ascorbic acid. The osteogenic medium was replaced every three days.

5.2.3.2. Alkaline phosphatase staining and Alizarin red s staining. After culturing in osteogenic medium for 7 days (n = 3), the mBMSCs of 2D models were rinsed three times with PBS, and fixed with 4% formaldehyde. An alkaline phosphatase staining kit (Gomori-modified calcium-cobalt method) was used according to the manufacturer's instructions (Solarbio, Beijing, China). The stained cells were examined with light microscopy (DM4000 B; Leica Microsystems).

After osteogenic induction for 14 days (n = 3), the mBMSCs in 35 mm dishes were washed and fixed following using the method described for Alizarin red S staining. A 0.2% Alizarin Red S staining solution (pH 8.3) was incubated with cells for 5 min. The stained cells were examined with light microscopy. The ImageJ image analysis software (National Institute of Health, Bethasda, MD, USA) was used for semi-quantitative analysis of alkaline phosphatase staining and Alizarin red S staining.

5.2.3.3. Reverse transcription-polymerase chain reaction (RT-PCR). Three osteogenesis-related genes were examined: Runt-related transcription factor 2 (Runx-2), osterix and osteocalcin. The primer sequences used for RT-PCR are shown in Supplementary Table S1. Ribonucleic acid was isolated using Trizol reagent and reverse-transcripted using the Prime Script RT reagent kit (Takara Bio Inc., Shiga, Japan). Real-time PCR (7500 Real-time PCR System; Applied Biosystems, Carlsbard, CA, USA) was performed with sense and antisense primers based on published cDNA sequences. Glyceraldehyde 3-phosphate dehydrogenase was used as the housekeeping gene. Fold changes relative to the control group were estimated using the $2^{-\triangle\triangle CT}$ method.

5.3. Regulation of the adaptive immune system in vivo

The rat alveolar bone defect model was implanted with Col and DNA-Col scaffolds. 6- to 8-week-old male Sprague-Dawley rats (n = 13) were used in this experiment. The rats were euthanized at 24 h after implant placement. The scaffolds with surrounding hematomas were collected and prepared for RNA sequencing, immunofluorescence, and flow cytometry.

5.3.1. Ribonucleic acid sequencing

Total RNA was extracted from the scaffolds and surrounding hematomas (n = 3). The Illumina HiSeq sequencing platform was used to obtain gene expression profiles. Quality control checks were performed to confirm sequencing saturation and gene mapping distribution. Fragments per kilobase of transcript per million mapped reads value were used to express relative gene abundance. To further examine the biological replicates between specimens, principal component analysis of the specimens was performed according to the expression levels of genes, using R software (https://www.r-project.org/).

Differential gene expression analysis was conducted using DESeq2 (https://bioconductor.org/). The result was defined as significantly changed if $P < 0.05$ and log2 (foldchange) $> |1|$. Hierarchical cluster analysis was performed using R software. The overall distribution of the differential genes was shown by the Volcano plot using ggplot2 R package. Gene ontology enrichment analysis of differentially expressed genes were respectively performed using R, based on hypergeometric distribution.

5.3.2. Immunofluorescence

Implants with surrounding clot were fixed in 4% paraformaldehyde (n = 6). The fixed specimens were embedded in paraffin, sliced into 4 μm-thick sections, and permeabilized in 0.15% Triton X-100. Regulatory T cells was stained with CD4 rabbit anti-rat antibody (500363, Zen-Bio, Inc., Durham, NC, USA) and Foxp3 mouse anti-rat antibody (2A11G9, Santa Cruz Biotechnology, Inc., Dallas, TX, USA). Alexa Fluor 488 goat anti-rabbit secondary antibody (33106ES60, Yeasen Biotechnology) and Alexa Fluor 594 goat anti-mouse secondary antibody (33212ES60, Yeasen Biotechnology) were used to label the primary antibodies. All specimens were rinsed and mounted with Prolong Diamond Antifade Mountant with 4′,6-diamidino-2-phenylindole (DAPI; Invitrogen, ThermoFisher Scientific). The images were captured using confocal laser-scanning microscopy (Nikon A1R, Nikon Corporation, Minato-ku, Tokyo, Japan). Relative fluorescence intensity was calculated using ImageJ software.

5.3.3. Flow cytometry

The DNA-Col and Col scaffolds with surrounding clot were extracted, and squeezed immediately through 70 μm filter to obtain single-cell suspensions (n = 4). Red blood cell lysis buffer (R1010, Solarbio) was used to deplete red blood cells. After lysis for 5 min, the single-cell suspensions were stained with surface markers: APC anti-rat CD4 antibody (201509, Biolegend, San Diego, CA, USA) and PE anti-rat CD25 antibody (202105, Biolegend). The single-cell suspensions were subsequently incubated with fixing and permeabilizing buffer (421403, Biolegend), and then stained with intracellular antibodies against Foxp3 (320012, Biolegend). Analysis of the stained cells was performed with a MoFloAstrios EQ flow cytometer (Beckman Coulter, Brea, CA, USA).

5.3.4. Treg depletion in vivo

Four-week-old male C57BL/6J mice were purchased from the Laboratory Animal Research Center of the Fourth Military Medical University. All surgical procedures were performed in compliance with the guidelines of the Laboratory Animal and Welfare Committee. Anti-mouse CD25 antibodies (PC-61.5.3, rat IgG1) and isotype control (HRPN, rat IgG1) were purchased from Bio X Cell (Lebanon, NH, USA). The amount of anti-CD25 antibodies used in the present study was 250 μg per mouse[58]. Treg depletion mice were used to detect depletion effect and osteogenesis with the sample size of n = 7. After 21 days, the depletion effect was examined using flow cytometry. The spleens of mice were mechanical ground on a 70 μm filter to obtain single-cell suspensions (n = 3). The single cells were stained with fluorescein isothiocyanate-conjugated anti-mouse CD4 antibody (96127S, Cell Signaling Technology, Danvers MA, USA) and phycoerythrin-conjugated anti-mouse Foxp3 antibody (E-AB-F1238D, Elabscience, Wuhan, Hubei, China), using the same method described in 5.3.3.

5.3.5. Murine alveolar bone defect model and micro-computed tomography

Alveolar bone defects were created in mice performed the day after Treg depletion. The mice were anesthetized with 1% pentobarbital sodium (50 mg/kg). The extraction steps were the same as extracting tooth of rats. After the maxillary right first molar was extracted, a Col or DNA-Col scaffold was implanted into the tooth socket. The maxillary bones of the euthanized mice were collected and fixed in 4% paraformaldehyde at the 21st day after surgery (n = 4). The specimens were scanned using the Inveon micro-CT, using the procedures described in section 5.2.2.

5.4. Regulation of Treg differentiation in vitro and in vivo

5.4.1. Regulation of Treg differentiation in vitro

5.4.1.1. Generation of in vitro inducible Tregs. The spleens of 6- to 8-week-old C57BL/6J mice (n = 20) were ground into single-cell suspensions. Lymphocytes from single-cell suspensions were isolated using density gradient centrifugation with lymphocyte separation medium (Dakewe Biotech, Shenzhen, China). Purification of CD4+T cells was performed using magnetic bead sorting (Biolegend) and confirmed with flow cytometry according to the manufacturer's instructions.

For *in vitro* Treg generation, the cells were seeded at 1×10^6 per well in an anti-CD3/CD28 antibody-coated 24-well plate (100340 and 102116, Biolegend). The PRMI-1640 medium for Treg differentiation contains 100 U/mL of IL-2 (PB180634, Pricella, Wuhan, Hubei, China) with TGF-β1 (HZ-1011, Proteintech) at 0.1 ng/mL. To explore the role of materials in the differentiation of Tregs, DNA-Col or Col scaffolds were added to the medium. T cells were incubated with 5% CO_2 at 37 °C and harvested 24 h later to evaluate Foxp3 expression.

5.4.1.2. Immunofluorescence. Harvested T cells were detected with Foxp3 mouse anti-mouse antibody (2A11G9, Santa Cruz) and Alexa Fluor 594 goat anti-mouse secondary antibody (33212ES60, Yeasen). The procedures were the same as 5.3.2 (n = 6).

5.4.1.3. Flow cytometry. Harvested T cells were stained with fluorescein isothiocyanate-conjugated anti-mouse CD4 antibody (96127S, Cell Signaling Technology). The stained cells were fixed and permeabilized according to the manufacturer's instructions (Biolegend), and stained with phycoerythrin-conjugated anti-mouse Foxp3 antibody (E-AB-F1238D, Elabscience), using the same method described in 5.3.3 (n = 6).

5.4.1.4. Enzyme-linked immunosorbent assay. The concentrations of the IL-4 and IL-10 in the supernatants of the co-culture system were determined using the IL-4 and IL-10 ELISA kits (E-EL-M0043c and E-EL-M0046c, Elabscience), respectively (n = 6).

5.4.1.5. Transmission electron microscopy. T cells incubated with DNA-Col and Col were pelleted at 800 g for 5 min. The pellets were fixed with 2.5% glutaraldehyde in phosphate buffer (0.01 M, pH 7.4) for 2 h at room temperature. The specimens were post-fixed with 1% osmium tetroxide, dehydrated with a graded ethanol series (30–100%), and embedded in Epon/Araldite resin mixture. Ninety nanometer–thick sections were cut with a diamond knife, mounted on 300-mesh copper grids, and stained with uranyl acetate and Reynold's lead citrate.

Sections were observed using a JEM-123 TEM (JEOL, Tokyo, Japan) at 110 kV.

5.4.1.6. Bioenergetic analyses. CD4+T cells were incubated with DNA-Col and Col in a RPMI-1640 medium with CD3/CD28 and IL-2 (n = 3). T cells were harvested after 24 h. The bioenergetic functions of the harvested T cells were measured using an XFe24 Analyzer (Seahorse Biosciences, North Billerica, MA, USA). To enable cell adherence, the XFe24 24-well plates were pre-coated with Cell-Tak (Corning Inc., Corning, NY, USA). The harvested CD4+T cells were seeded at a concentration of 0.5 million/100 μL XF assay medium containing 1 mM of pyruvate, 2 mM of glutamine, and 10 mM of glucose at pH 7.4, and then incubated at 37 ℃ in a non-CO_2 incubator. An additional 350 μL of assay medium was added to each well after 30 min. For oxygen consumption rate evaluation, oligomycin, carbonyl cyanide-4-(trifluoromethoxy) phenylhydrazone, rotenone, and antimycin A were injected sequentially through ports of the Seahorse Flux Pak cartridges to reach final concentrations of 1.0 μM, 2.5 μM, and 1 μM, respectively. For evaluation of extracellular acidification rate, glucose, oligomycin, and 2-deoxy-D-glucose were added subsequently to reach final concentrations of 100 mM, 10 μM, and 500 mM, respectively.

5.4.1.7. Inhibition of TLR4. The CD4+T cells were pretreated *in vitro* with 10 nM of resatorvid (TAK-242) (MCE, Monmouth Junction, NJ, United States) for 3 h to inhibit TLR4 activity prior to seeding into 24-well plates. The plates were pre-coated with CD3/CD28. CD4+T cells without TAK-242 was used as control. The DNA-Col or Col scaffold was added to 24-well plates, and incubated with T cells for 24 h.

5.4.1.8. Immunofluorescence. The DNA-Col or Col scaffold was added to CD4+T cells of the control group and the TLR4 inhibition group. The T cells were harvested after 24 h and fixed in 4% paraformaldehyde. After rinsing three times with PBS, 0.15% Triton X-100 was added to the centrifuged T cells pellets. The T cells were subsequently stained with fluorescein isothiocyanate-conjugated rat anti-mouse CD4 antibody (96127S, Cell Signaling Technology) and mouse anti-mouse PGC-1α antibody (66369–1-Ig, Proteintech). Alexa Fluor 594 goat anti-mouse secondary antibody (33212ES60, Yeasen) was used to bind primary antibodies. For measurement of fluorescence intensity, cells that were positive to CD4 and PGC-1α were manually selected and analyzed using the ImageJ software.

5.4.1.9. Western blot. Western blot was used to identify the expression of PGC-1α, phosphorylated p38 (p-p38), and total p38 (p38) in the control and TLR4 inhibition groups (n = 3). After culturing for 24 h with DNA-Col and Col, T cells were collected and lysed with protein extraction reagent that was supplemented with a protease inhibitor cocktail (Thermo Fisher Scientific). Protein specimens were separated with a 10% SDS-polyacrylamide gel and transferred onto polyvinylidene difluoride membranes (MilliporeSigma). Each membrane was blocked with 5% bovine serum albumin and incubated with primary antibodies overnight at 4 °C. The primary antibodies were anti-PGC-1α, anti-p-p38, anti-p38, and anti-β-actin (1:1000; Cell Signaling Technology). Signals were revealed after incubation with horseradish peroxidase-conjugated secondary antibody (1:5000, Servicebio, Wuhan, Hubei, China) and enhanced chemiluminescence detection (GeneTex, Irvine CA, USA). The stained bands were scanned and quantified using a densitometer (Tanon, Shanghai, China) and the ImageJ software. Protein expressions were normalized against β-actin.

5.4.2. Regulation of Treg differentiation in vivo

5.4.2.1. Alveolar bone defect model in TLR4-inhibited mice. Four-week-old male C57BL/6J mice were pretreated with intraperitoneal injection of TAK-242 (3 mg/kg) with the sample size of n = 4. The maxillary right first molar was extracted 30 min after injection. The Col or DNA-Col scaffold was implanted into the tooth socket.

5.4.2.2. In vivo flow cytometry. Animals were euthanized 24 h after implant placement. The scaffolds with surrounding hematomas were harvested to collect the single-cell suspensions (n = 4). Flow cytometry was performed in the manner described in 5.3.3.

5.5. Statistical analysis

All data were presented as means ± standard deviations. The Shapiro-Wilk test was used to test for the normality assumption of the corresponding data sets. The modified Levene test was used to test the homogeneity of variance assumption of the corresponding data sets. Parametric statistical tests were used after validating that those two assumptions were not violated. Comparisons between 2 groups were examined using Student's *t*-test. Comparisons involving more than 2 groups were analyzed using one-way analysis of variance. The GraphPad Prism 8 package (GraphPad Software, La Jolla, CA, USA) was used for analyses. For all analyses, statistical significance was pre-set at $\alpha = 0.05$.

Declaration of Competing Interest

The authors declare that they have no known competing financial interests or personal relationships that could have appeared to influence the work reported in this paper.

Data availability

The data that has been used is confidential.

Acknowledgments

This work is supported by the National Key R&D Program of China (Grant No. 2022YFC2405900, 2022YFC2405901), the National Natural Science Fundation of China (Grant No. 82325012, 82301043, 81870805), and the Shaanxi Key Scientific and Technological Innovation Team (Grant No. 2020TD-033). The authors thank Figdraw (https://www.figdraw.com/) and Biorender (https://www.biorender.com/) for their help in creating the schematic illustrations. The authors also thank Shanghai Bioprofile Technology Company Ltd for technological assistance in RNA-sequence experiment.

Appendix A. Supplementary data

Supplementary data to this article can be found online at https://doi.org/10.1016/j.cej.2023.145318.

References

[1] D. Lopes, C. Martins-Cruz, M.B. Oliveira, J.F. Mano, Bone physiology as inspiration for tissue regenerative therapies, Biomaterials 185 (2018) 240–275, https://doi.org/10.1016/j.biomaterials.2018.09.028.
[2] C. Lei, J.H. Song, S. Li, Y.N. Zhu, M.Y. Liu, M.C. Wan, Z. Mu, F.R. Tay, L.N. Niu, Advances in materials-based therapeutic strategies against osteoporosis, Biomaterials 296 (2023), 122066, https://doi.org/10.1016/j.biomaterials.2023.122066.
[3] G.L. Koons, M. Diba, A.G. Mikos, Materials design for bone-tissue engineering, Nature Reviews Materials 5 (2020) 584–603, https://doi.org/10.1038/s41578-020-0204-2.
[4] M.N. Collins, G. Ren, K. Young, S. Pina, R.L. Reis, J.M. Oliveira, Scaffold Fabrication Technologies and Structure/Function Properties in Bone Tissue Engineering, Advanced Functional Materials 31 (2021) 2010609, https://doi.org/10.1002/adfm.202010609.
[5] C.I. Codrea, A.M. Croitoru, C.C. Baciu, A. Melinescu, D. Ficai, V. Fruth, A. Ficai, Advances in Osteoporotic Bone Tissue Engineering, Journal of Clinical Medicine 10 (2021) 253, https://doi.org/10.3390/jcm10020253.
[6] C.Y. Wang, Z.X. Qin, Y. Wei, J.X. Hao, Y.F. Zhu, F. Zhao, K. Jiao, H. Ehrlich, F. R. Tay, L.N. Niu, The immunomodulatory effects of RNA-based biomaterials on

bone regeneration, Acta Biomaterialia 162 (2023) 32–43, https://doi.org/10.1016/j.actbio.2023.03.031.
[7] M.-J. Shen, C.-y. Wang, D.-X. Hao, J.-X. Hao, Y.-F. Zhu, X.-X. Han, L. Tonggu, J.-H. Chen, K. Jiao, F.R. Tay, L.-n. Niu, Multifunctional Nanomachinery for Enhancement of Bone Healing, Advanced Materials 34 (9) (2022), e2107924, https://doi.org/10.1002/adma.202107924.
[8] C. Wang, W. Huang, Y. Zhou, L.B. He, Z. He, Z.L. Chen, X. He, S. Tian, J.M. Liao, B. H. Lu, Y. Wei, M. Wang, 3D printing of bone tissue engineering scaffolds, Bioactive Materials 5 (2020) 82–91, https://doi.org/10.1016/j.bioactmat.2020.01.004.
[9] W.J. Zhang, M.L. Yu, Y.Q. Cao, Z.H. Zhuang, K.X. Zhang, D. Chen, W.G. Liu, J. B. Yin, An anti-bacterial porous shape memory self-adaptive stiffened polymer for alveolar bone regeneration after tooth extraction, Bioactive Materials 21 (2023) 450–463, https://doi.org/10.1016/j.bioactmat.2022.08.030.
[10] M. Farmer, I. Darby, Ridge dimensional changes following single-tooth extraction in the aesthetic zone, Clinical Oral Implants Research 2 (2014) 272–277, https://doi.org/10.1111/clr.12108.
[11] E. Couso-Queiruga, S. Stuhr, M. Tattan, L. Chambrone, G. Avila-Ortiz, Post-extraction dimensional changes: A systematic review and meta-analysis, Journal of Clinical Periodontology 48 (2021) 126–144, https://doi.org/10.1111/jcpe.13390.
[12] G. Nechifor, E. Eftimie Totu, A.C. Nechifor, I. Isildak, O. Oprea, C.M. Cristache, Non-Resorbable Nanocomposite Membranes for Guided Bone Regeneration Based On Polysulfone-Quartz Fiber Grafted with Nano-TiO_2, Nanomaterials 9 (7) (2019) 985.
[13] F.L. Wang, D.D. Xia, S.Y. Wang, R.L. Gu, F. Yang, X. Zhao, X.N. Liu, Y. Zhu, H. Liu, Y.X. Xu, Y.S. Liu, Y.S. Zhou, Photocrosslinkable Col/PCL/Mg composite membrane providing spatiotemporal maintenance and positive osteogenetic effects during guided bone regeneration, Bioactive Materials 13 (2022) 53–63, https://doi.org/10.1016/j.bioactmat.2021.10.019.
[14] A.S. Kalsi, J.S. Kalsi, S. Bassi, Alveolar ridge preservation: why, when and how, British Dental Journal 227 (2019) 264–274, https://doi.org/10.1038/s41415-019-0647-2.
[15] G.T. Tihan, I. Rău, R.G. Zgârian, C. Ungureanu, R.C. Barbaresso, M.G.A. Kaya, C. Dinu-Pîrvu, M.V. Ghica, Oxytetracycline versus Doxycycline Collagen Sponges Designed as Potential Carrier Supports in Biomedical Applications, Pharmaceutics. 11 (2019) 363, https://doi.org/10.3390/pharmaceutics11080363.
[16] B. Manavalan, S. Basith, T.H. Shin, G. Lee, Computational prediction of species-specific yeast DNA replication origin via iterative feature representation, Briefings in Bioinformatics 22 (2021) bbaa304, https://doi.org/10.1093/bib/bbaa304.
[17] R. Kim, S. Kanamaru, T. Mikawa, C. Prévost, K. Ishii, K. Ito, S. Uchiyama, M. Oda, H. Iwasaki, S.K. Kim, M. Takahashi, RecA requires two molecules of Mg2+ ions for its optimal strand exchange activity in vitro, Nucleic Acids Research. 46 (2018) 2548–2559, https://doi.org/10.1093/nar/gky048.
[18] A. Chakraborty, S.P. Ravi, Y. Shamiya, C. Cui, A. Paul, Harnessing the physicochemical properties of DNA as a multifunctional biomaterial for biomedical and other applications, Chemical Society Reviews 50 (2021) 7779–7819, https://doi.org/10.1039/d0cs01387k.
[19] T. Sakurai, M. Yoshinari, T. Toyama, T. Hayakawa, C. Ohkubo, Effects of a multilayered DNA/protamine coating on titanium implants on bone responses, Journal of Biomedical Materials Research. Part A 104 (2016) 1500–1509, https://doi.org/10.1002/jbm.a.35679.
[20] M.J. Shen, K. Jiao, C.Y. Wang, H. Ehrlich, M.C. Wan, D.X. Hao, J. Li, Q.Q. Wan, L. Tonggu, J.F. Yan, K.Y. Wang, Y.X. Ma, J.H. Chen, F.R. Tay, L.N. Niu, Extracellular DNA: A Missing Link in the Pathogenesis of Ectopic Mineralization, Advancement of Science 9 (2022) e2103693.
[21] A.L. Danesi, D. Athanasiadou, A.O. Aderinto, P. Rasie, L.Y.T. Chou, K.M. M. Carneiro, Peptide-Decorated DNA Nanostructures Promote Site-Specific Hydroxyapatite Growth, ACS Applied Materials & Interfaces 14 (2022) 1692–1698, https://doi.org/10.1021/acsami.1c19271.
[22] X.G. Liu, X.X. Jing, P. Liu, M.C. Pan, Z. Liu, X.P. Dai, J.P. Lin, Q. Li, W. Fei, S. C. Yang, L.H. Wang, C.H. Fan, DNA Framework-Encoded Mineralization of Calcium Phosphate, Chem 6 (2020) 472–485, https://doi.org/10.1016/j.chempr.2019.12.003.
[23] D. Athanasiadou, N. Meshry, N.G. Monteiro, A.C. Ervolino-Silva, R.L. Chan, C. A. McCulloch, R. Okamoto, K.M.M. Carneiro, DNA hydrogels for bone regeneration, Proceedings of the National Academy of Sciences of the United States of America 120 (2023), https://doi.org/10.1073/pnas.2220565120 e2220565120.
[24] Y.H. Wei, K.Z. Wang, S.H. Luo, F. Li, X.L. Zuo, C.H. Fan, Q. Li, Programmable DNA Hydrogels as Artificial Extracellular Matrix, Small 18 (2022) e2107640.
[25] F. Ding, S.Y. Zhang, Q. Chen, H. Feng, Z.L. Ge, X.L. Zuo, C.H. Fan, Q. Li, Q. Xia, Immunomodulation with Nucleic Acid Nanodevices, Small 19 (2023) e2206228.
[26] W.J. Ma, Y.X. Zhan, Y.X. Zhang, C.C. Mao, X.P. Xie, Y.F. Lin, The biological applications of DNA nanomaterials: current challenges and future directions, Sig Transduct Target Ther. 6 (2021) 351, https://doi.org/10.1038/s41392-021-00727-9.
[27] B. Duan, P.F. Ding, T.R. Hughes, W.W. Navarre, J. Liu, B. Xia, How bacterial xenogeneic silencer rok distinguishes foreign from self DNA in its resident genome, Nucleic Acids Research 46 (2018) 10514–10529, https://doi.org/10.1093/nar/gky836.
[28] J.J. van den Beucken, M.R. Vos, P.C. Thüne, T. Hayakawa, T. Fukushima, Y. Okahata, X.F. Walboomers, N.A. Sommerdijk, R.J. Nolte, J.A. Jansen, Fabrication, characterization, and biological assessment of multilayered DNA-coatings for biomaterial purposes, Biomaterials 27 (2006) 691–701, https://doi.org/10.1016/j.biomaterials.2005.06.015.
[29] J.T. Gu, K. Jiao, J. Li, J.F. Yan, K.Y. Wang, F. Wang, Y. Liu, F.R. Tay, J.H. Chen, L. N. Niu, Polyphosphate-crosslinked collagen scaffolds for hemostasis and alveolar bone regeneration after tooth extraction, Bioactive Materials 15 (2022) 68–81, https://doi.org/10.1016/j.bioactmat.2021.12.019.
[30] H.Y. Chen, Y. Chen, H.B. Liu, Y. Que, X. Zhang, F. Zheng, Integrated Expression Profiles Analysis Reveals Correlations Between the IL-33/ST2 Axis and CD8(+) T Cells, Regulatory T Cells, and Myeloid-Derived Suppressor Cells in Soft Tissue Sarcoma, Frontiers in Immunology 9 (2018) 1179, https://doi.org/10.3389/fimmu.2018.01179.
[31] G. Mijnheer, L. Lutter, M. Mokry, M. van der Wal, R. Scholman, V. Fleskens, A. Pandit, W. Tao, M. Wekking, S. Vervoort, C. Roberts, A. Petrelli, J.G.C. Peeters, M. Knijff, S. de Roock, S. Vastert, L.S. Taams, J. van Loosdregt, F. van Wijk, Conserved human effector Treg cell transcriptomic and epigenetic signature in arthritic joint inflammation, Nature Communications 12 (2021) 2710, https://doi.org/10.1038/s41467-021-22975-7.
[32] M.G. Strainic, J. Liu, F. An, E. Bailey, A. Esposito, J. Hamann, P.S. Heeger, M. E. Medof, CD55 Is Essential for CD103(+) Dendritic Cell Tolerogenic Responses that Protect against Autoimmunity, The American Journal of Pathology 189 (2019) 1386–1401, https://doi.org/10.1016/j.ajpath.2019.04.008.
[33] J.R. Dwyer, J.J. Racine, H.D. Chapman, A. Quinlan, M. Presa, G.A. Stafford, I. Schmitz, D.V. Serreze, Nfkbid Overexpression in Nonobese Diabetic Mice Elicits Complete Type 1 Diabetes Resistance in Part Associated with Enhanced Thymic Deletion of Pathogenic CD8 T Cells and Increased Numbers and Activity of Regulatory T Cells, Journal of Immunology 209 (2) (2022) 227–237.
[34] M. Andreatta, J. Corria-Osorio, S. Müller, R. Cubas, G. Coukos, S.J. Carmona, Interpretation of T cell states from single-cell transcriptomics data using reference atlases, Nature Communications 12 (2021) 2965, https://doi.org/10.1038/s41467-021-23324-4.
[35] F. Sun, T.T. Yue, C.L. Yang, F.X. Wang, J.H. Luo, S.J. Rong, M. Zhang, Y. Guo, F. Xiong, C.Y. Wang, The MAPK dual specific phosphatase (DUSP) proteins: A versatile wrestler in T cell functionality, International Immunopharmacology. 98 (2021), 107906, https://doi.org/10.1016/j.intimp.2021.107906.
[36] H.M. Chen, W. van der Touw, Y.S. Wang, K. Kang, S. Mai, J. Zhang, D. Alsina-Beauchamp, J.A. Duty, S.K. Mungamuri, B. Zhang, T. Moran, R. Flavell, S. Aaronson, H.M. Hu, H. Arase, S. Ramanathan, R. Flores, P.Y. Pan, S.H. Chen, Blocking immunoinhibitory receptor LILRB2 reprograms tumor-associated myeloid cells and promotes antitumor immunity, The Journal of Clinical Investigation 128 (2018) 5647–5662, https://doi.org/10.1172/jci97570.
[37] M.E. Schober, D.F. Requena, T.C. Casper, A.K. Velhorst, A. Lolofie, K.E. McFarlane, T.E. Otto, C. Terry, J.C. Gensel, Docosahexaenoic acid decreased neuroinflammation in rat pups after controlled cortical impact, Experimental Neurology 320 (2019), 112971, https://doi.org/10.1016/j.expneurol.2019.112971.
[38] J. Wu, Y.P. Wang, Role of TNFSF9 bidirectional signal transduction in antitumor immunotherapy, European Journal of Pharmacology 928 (2022), 175097, https://doi.org/10.1016/j.ejphar.2022.175097.
[39] M. Colonna, TREMs in the immune system and beyond, Nature Reviews. Immunology 3 (2003) 445–453, https://doi.org/10.1038/nri1106.
[40] J. Ford, A. Hughson, K. Lim, S.V. Bardina, W. Lu, I.F. Charo, J.K. Lim, D.J. Fowell, CCL7 Is a Negative Regulator of Cutaneous Inflammation Following Leishmania major Infection, Frontiers in Immunology 9 (2018) 3063, https://doi.org/10.3389/fimmu.2018.03063.
[41] S.S. Feng, Z.G. Xu, Z.G. Zhang, Y.Q. Mo, Y.Y. Deng, L. Li, S.T. Fei, J.M. Wu, K. F. Wang, Q.W. Zhang, J. Song, R.X. Zhou, RNA-Seq approach to investigate the effects of melatonin on bone marrow-derived dendritic cells from dextran sodium sulfate-induced colitis mice, Toxicology 481 (2022), 153354, https://doi.org/10.1016/j.tox.2022.153354.
[42] T. Ono, M. Hayashi, F. Sasaki, T. Nakashima, RANKL biology: bone metabolism, the immune system, and beyond, Inflamm Regen. 40 (2022) 2, https://doi.org/10.1186/s41232-019-0111-3.
[43] J.H. Lee, B. Kim, W.J. Jin, H.H. Kim, H. Ha, Z.H. Lee, Pathogenic roles of CXCL10 signaling through CXCR3 and TLR4 in macrophages and T cells: relevance for arthritis, Arthritis Research & Therapy 19 (2017) 163, https://doi.org/10.1186/s13075-017-1353-6.
[44] L.i. Yi, G. Guo, J. Li, X. Fan, T. Li, L. Tong, P. Liu, X. Wang, F. Yuan, S. Yu, Q. Huang, X. Yang, IKBKE, a prognostic factor preferentially expressed in mesenchymal glioblastoma, modulates tumoral immunosuppression through the STAT3/PD-L1 pathway, Clinical and Translational Medicine 10 (3) (2020) e130.
[45] H. Wang, H. Zhang, Y. Wang, Z.J. Brown, Y. Xia, Z. Huang, C. Shen, Z. Hu, J. Beane, E.A. Ansa-Addo, H. Huang, D. Tian, A. Tsung, Regulatory T-cell and neutrophil extracellular trap interaction contributes to carcinogenesis in non-alcoholic steatohepatitis, Journal of Hepatology 75 (2021) 1271–1283, https://doi.org/10.1016/j.jhep.2021.07.032.
[46] L. Almeida, A. Dhillon-LaBrooy, G. Carriche, L. Berod, T. Sparwasser, CD4(+) T-cell differentiation and function: Unifying glycolysis, fatty acid oxidation, polyamines NAD mitochondria, The Journal of Allergy and Clinical Immunology 148 (2021) 16–32, https://doi.org/10.1016/j.jaci.2021.03.033.
[47] H.O. Yazdani, A.J. Comerci, D.J. van der Windt, H. Zhang, H. Huang, P. Loughran, S. Shiva, D.A. Geller, D.L. Bartlett, A. Tsung, T. Sheng, R.L. Simmons, S. Tohme, Neutrophil Extracellular Traps Drive Mitochondrial Homeostasis in Tumors to Augment Growth, Cancer Research 79 (21) (2019) 5626–5639, doi: 10.1158/0008-5472.
[48] L.R. Prince, M.K. Whyte, I. Sabroe, L.C. Parker, The role of TLRs in neutrophil activation, Current Opinion in Pharmacology 11 (2011) 397–403, https://doi.org/10.1016/j.coph.2011.06.007.
[49] L. Gu, T. Shan, Y.X. Ma, F.R. Tay, L.N. Niu, Novel Biomedical Applications of Crosslinked Collagen, Trends in Biotechnology 37 (2019) 464–491, https://doi.org/10.1016/j.tibtech.2018.10.007.

[50] P. Shen, Y.X. Chen, S. Luo, Z.Y. Fan, J.L. Wang, J. Chang, J.J. Deng, Applications of biomaterials for immunosuppression in tissue repair and regeneration, Acta Biomaterialia 126 (2021) 31–44, https://doi.org/10.1016/j.actbio.2021.03.019.
[51] L. Claes, S. Recknagel, A. Ignatius, Fracture healing under healthy and inflammatory conditions, Nature Reviews Rheumatology 8 (2012) 133–143, https://doi.org/10.1038/nrrheum.2012.1.
[52] K. Schmidt-Bleek, H. Schell, J. Lienau, N. Schulz, P. Hoff, M. Pfaff, G. Schmidt, C. Martin, C. Perka, F. Buttgereit, H.D. Volk, G. Duda, Initial immune reaction and angiogenesis in bone healing, Journal of Tissue Engineering and Regenerative Medicine 8 (2014) 120–130, https://doi.org/10.1002/term.1505.
[53] H. Jiang, Y.F. Ti, Y.C. Wang, J. Wang, M.H. Chang, J.N. Zhao, G.J. Sun, Downregulation of regulatory T cell function in patients with delayed fracture healing, Clinical and Experimental Pharmacology & Physiology 45 (2018) 430–436, https://doi.org/10.1111/1440-1681.12902.
[54] Y. Liu, L. Wang, T. Kikuiri, K. Akiyama, C. Chen, X.T. Xu, R.L. Yang, W.J. Chen, S. L. Wang, S.T. Shi, Mesenchymal stem cell–based tissue regeneration is governed by recipient T lymphocytes via IFN-γ and TNF-α, Nature Medicine 17 (2011) 1594–1601, https://doi.org/10.1038/nm.2542.
[55] A. Bozec, M.M. Zaiss, T Regulatory Cells in Bone Remodelling, Current Osteoporosis Reports 15 (2017) 121–125, https://doi.org/10.1007/s11914-017-0356-1.
[56] R. Ventura-Clapier, A. Garnier, V. Veksler, Transcriptional control of mitochondrial biogenesis: the central role of PGC-1alpha, Cardiovascular Research 79 (2008) 208–217, https://doi.org/10.1093/cvr/cvn098.
[57] J.M. González-Navajas, S. Fine, J. Law, S.K. Datta, K.P. Nguyen, M. Yu, M. Corr, K. Katakura, L. Eckman, J. Lee, E. Raz, TLR4 signaling in effector CD4+ T cells regulates TCR activation and experimental colitis in mice, The Journal of Clinical Investigation 120 (2010) 570–581, https://doi.org/10.1172/jci40055.
[58] R. Shanmugasundaram, R.K. Selvaraj, Effects of in vivo injection of anti-chicken CD25 monoclonal antibody on regulatory T cell depletion and CD4+CD25- T cell properties in chickens, Developmental and Comparative Immunology 36 (2012) 578–583, https://doi.org/10.1016/j.dci.2011.09.015.